

Numerical Simulation of Heat Transfer in Miniature Radially Rotating **Sodium/Potassium Heat Pipes**

Guo Li1^{1,2}, Yuchen Zhang1^{2,*}, Guohua Zhang3³, Shiyu Huang4³ & Shuiting Ding5⁴

¹Tianmushan Laboratory (Zhejiang Provincial Laboratory for Aviation), Hangzhou 311121, China 1 ²School of Energy and Power Engineering, Beihang University, Beijing 100191, China 2 ³Research Institute of Aero-Engine, Beihang University, Beijing 100191, China 3 ⁴Civil Aviation University of China, Tianjin 300300, China 4

Abstract

The turbine disks and compressor disks are the life limiting components of aero-engines. As the increasing of pressure ratio and temperature rise ratio, these components are exposed to more demanding thermal loads. One potential solution to enhance thermal protection performance is the utilization of radially rotating heat pipes (RRHP) that have efficient thermal conductivity. However, it is necessary to study the heat transfer performance of RRHP under high temperature and high-speed conditions in aero-engines. This study establishes a numerical simulation model of miniature sodium/potassium RRHPs is to predict their heat transfer characteristics and two-phase flow inside. The RRHP simulation results are compared with changes in centrifugal acceleration ranging from 100 g to 10000 g, liquid filling ratio from 50% to 100%, and heat power from 120 W to 360 W. The results show that the effective thermal conductivity of RRHPs slightly decreases with increasing rotating speed. However, the equivalent thermal resistance of RRHPs increases by no more than 10%. Additionally, a higher liquid filling ratio is required at high speeds to prevent local overheating. When the centrifugal acceleration is 5000 g, the equivalent thermal resistance and equivalent thermal conductivity of the sodium and potassium heat pipe can reach 9176 W/m·K and 8966 W/m·K, respectively.

Keywords: Thermal management, Radially rotating heat pipe, High temperature, Liquid alkali metal, Heat transfer

1. Introduction

In recent years, there has been a growing demand for supersonic civil aviation aircraft, resulting in increased requirements for aero-engine performance. The main way to improve the performance of aviation gas turbine engines is by increasing the pressure ratio and temperature rise ratio. Consequently, the compressor system and turbine system are exposed to increasingly complex thermal loads, with compressor outlet temperatures exceeding 1000 K and turbine inlet temperatures surpassing 2000 K [1]. These challenging thermal conditions impose strict demands on thermal management. As the most crucial life limiting components of aero-engine, both compressor disks and turbine disks are subjected to extreme centrifugal and thermal loads [2]. Therefore, it is crucial to develop a new design concept for thermal management technology to ensure the future advancement of aviation engines.

The thermal stress of a disk is caused by the temperature gradient generated from uneven heating. In the past, the compressor disks were subjected to low temperatures due to the compressed air, resulting in lower levels of thermal stress. However, as the total pressure ratio and flight speed have increased, the outlet airflow of the compressor now reaches extremely high temperatures. As a

result, the thermal load on the high-pressure stage disk of the compressor cannot be ignored. Currently, the primary method of thermal protection for aero-engine turbines involves injecting air from the compressor to reduce surface temperature. This approach effectively reduces the maximum temperature and temperature gradient to meet the durability and lifespan requirements of the materials, while also alleviating thermal stress [3,4]. Researchers have proposed various cooling structures for turbine disks [5-8], such as adding pre-swirl nozzles, and the adjusting nozzle positions to decrease the temperature and enhance the disk surface heat transfer coefficient. These methods have successfully reducd the maximum temperature and temperature gradient, achieving the objective of thermal protection. However, current aero-engines require a significant amount of cooling air, approximately 20% to 25% of the total airflow, and the development of traditional cooling methods is reaching its limits [9]. Therefore, it is an urgent need to propose a new thermal management technology that can ensure a more efficient distribution of energy within the disk.

Cao et al. [10] emphasized the significant role of low thermal conductivity in superalloys, which negatively affects turbine performance. In response, Ding et al. [11] introduced an active thermal management approach involving disk center heating. This method effectively reduced maximum stress levels by creating a reverse temperature gradient. However, implementing disk center heating necessitated the addition of another gas path, which increases structural complexity and weight. Considering the exceptional thermal conductivity, isothermal properties, and structural versatility of heat pipes, they have become an attractive solution in the aero-engine industry. Heat pipes exhibit thermal conductivity 60-100 times higher than copper [12]. Keeping this in mind, a heat pipe turbine disk (HPD) was proposed to enhance aero-engine performance [13-15]. This novel thermal management method combines the traditional air-cooling technique with radially rotating miniature high-temperature heat pipes for gas turbine cooling. Embedded RRHPs are achieved through disk slotting, and different liquid metals are filled as working fluids based on the usage temperature. The disk serves as the outer shell of RRHPs, facilitating heat transfer through liquid metal phase change. The working fluid absorbs heat and evaporates in the evaporation section at the disk rim. The vapor is then propelled to the condenser section due to the pressure gradient. At the condensation section located at the disk hub, the vapor releases heat and condenses, causing the liquid working fluid to be driven to the evaporator section by the centrifugal force of rotation. The energy is transferred through the cyclic phase change of the working fluid. The working principle of the RRHP is illustrated in Figure. 1.

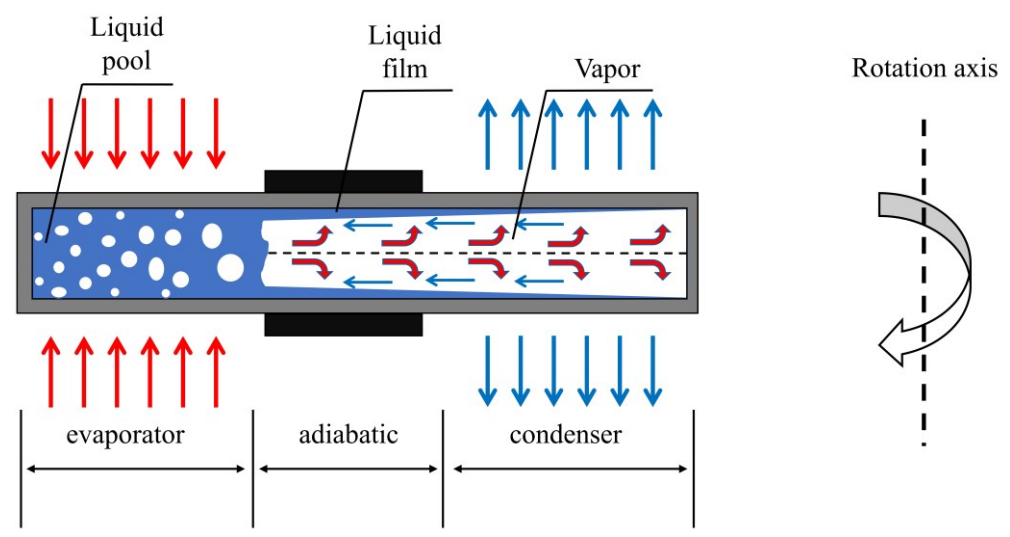


Figure 1. Working principle of the RRHP

High temperature heat pipes typically utilized alkali metals such as potassium, sodium, and lithium as working fluids [16]. Potassium heat pipes are capable of operating within a temperature range of 600-1000 K, making them ideal for high-pressure compressor disks. Sodium heat pipes can operate at higher temperatures, specifically between 800-1300 K [17], making them suitable for

turbine disks. Therefore, this research focused on sodium and potassium high-temperature RRHPs to investigate their potential application in thermal management for high-speed rotating machinery.

Ling et al.[18] developed the theory of high-temperature RRHPs based on the principles of thermosyphons. They also established the theory of liquid film distribution and vapor flow inside the RRHPs, and analyzed the potential use of micro high-temperature RRHPs in gas turbines. In their research, sodium was used as the working fluid in the micro high-temperature RRHPs. The results demonstrated that these high-temperature RRHPs would not encounter the condensation heat transfer limitation typically seen in heat pipes operating at lower temperatures. However, the calculation methods used were relatively simple and had some limitations. These limitations were mainly observed in three aspects: Firstly, the influence of the thermal conductivity of the heat pipe shell on the heat transfer characteristics was not taken into consideration. Secondly, the RRHP theory did not calculate the heat transfer coefficient of the evaporator section. Lastly, the RRHP theory could not account for the possible liquid carrying limitation. Conducting experimental research on hightemperature RRHPs presented significant challenges, particularly in replicating the rotational speed of aircraft engines in laboratory conditions. This required ensuring high levels of experimental safety, as well as substantial time and financial costs. Consequently, only a few experimental studies were conducted on high-temperature RRHPs, and the measuring and testing techniques used were relatively simple. For example, only 5 temperature points were obtained from the heat pipe shell, which was insufficient to fully capture the actual working conditions of the RRHP.

In recent years, computational fluid dynamics (CFD) technology has become increasingly popular in the study of heat pipes. This approach has proven to be effective and economical, providing researchers with valuable visualization capabilities to obtain information about flow and heat transfer. As a result, scholars have focused on conducting numerical simulation research on two types of heat pipes: radially rotating heat pipes (RRHPs) [19-21] and high-temperature alkali metal heat pipes [22-25]. For RRHPs, Chen et al.[19] conducted a simulation to study the heat transfer mechanism in the evaporator and condenser sections of a RRHP grinding wheel with a velocity of 45 m/s. The results indicated that natural convection heat transfer and film condensation occurred under these conditions. The RRHP demonstrated excellent heat transfer performance at high speeds. Qian et al. [20] developed a radially rotating oscillating heat pipe (RR-OHP) that used methanol and DI water as working fluid to enhance the heat performance of the grinding wheel. The results showed that increasing the heat flux and centrifugal acceleration could improve the thermal performance of RR-OHPs. Luo et al.[21] investigated the effects of vapor-liquid phase change in axially rotating heat pipes on the fluid-thermal-solid behaviors of high-speed spindles through numerical simulations and experiments. They examined the operational and heat dissipation performance of the rotating heat pipe under various operating conditions and analyzed the effects of speed, heat flux, and cooling air flow rate.

For high-temperature heat pipes, Sun et al. [22,23] utilized Fluent software to simulate the evaporation and condensation process of alkali metal heat pipes in a specific layer of the grid. Commercial software, including user defined functions (UDFs), was used to obtain the temperature and flow field inside the heat pipe. The methodology was validated with experimental data, demonstrating that the calculation model accurately simulated the thermal-hydraulic characteristics of potassium heat pipes. Dutra et al.[24] constructed the actual geometry of the wick structure in a heat pipe and simulated the liquid within the wick. However, the small wick diameter (less than 0.1 mm) required significant computing resources. Zhang et al. [25] developed a three-stage frozen startup model to describe the thermal behavior of high-temperature heat pipes during the startup process. They implemented a numerical code using the Finite Element Method (FEM) and used the model to simulate the startup performance of a Na-K heat pipe cooled reactor. The numerical results indicated that this model accurately described the heat pipe startup behavior.

The research mentioned above suggests that the CFD method is successful in simulating vaporliquid flow and phase change processes under high centrifugal acceleration. However, current numerical simulations of high-temperature heat pipes mainly focus on wick-type heat pipes. There is currently no specific model that can be used to analyze the numerical simulation of heat pipes that use rotational centrifugal force as the driving force for liquid metal reflux. Hence, the aim of this study is to develop a universal model that can be applied to steady-state heat transfer in high-temperature RRHPs. In Section 2, the governing equations for the two-phase flow model and phase change model used in numerical simulation were introduced. The UDF is utilized to incorporate source terms for simulating evaporation process, condensation process, and the application of centrifugal force. Next, in Section 3 the two-dimensional simulation model of the RRHP was introduced. And the mesh independence testing was conducted to determine appropriate mesh strategies. In Section 4, some preliminary research results were presented. The study investigated the heat transfer performance of two types of high-temperature RRHPs under varying rotational centrifugal accelerations, heating conditions, and filling ratios. The findings demonstrated that the model was suitable for solving heat and mass transfer processes in heat pipes under high rotational centrifugal acceleration.

2. The CFD numerical model

The aim of this study was to investigate the micro rotational centrifugal force heat pipe (RRHP) at high temperatures. This type of heat pipe utilizes rotational centrifugal force to enhance the flow of the liquid working fluid, thus eliminating the need for a wick. Therefore, the study primarily examined the heat and mass transfer process at the phase change interface and the influence of centrifugal force on the model parameters. It is important to note that this study exclusively concentrated on the steady-state performance of high-temperature RRHP, and did not address the common start-up issue encountered in high-temperature heat pipes.

2.1 Governing equations

The VOF model [26] is a Euler–Euler model commonly used for solving multiphase problems. It is used to determine the motion of all phases and define the motion of the interfaces. The VOF technique is applicable for modeling two immiscible fluids with a well-defined interface between the phases. It is also employed for surface-tracking in a fixed mesh. The VOF method is based on the phase volume fraction α , which ranges from 0 to 1 for each phase. It is used to monitor the vapor-liquid interface. The phase volume fraction is calculated using the following equation:

$$\frac{\partial}{\partial t}(\alpha) + \vec{i} \qquad (1)$$

The volume fraction α of phase is defined as follows.

 $\alpha_l = 1$: The cell is full of liquid.

 $\alpha_{v} = 1$: The cell is full of vapor

 $0 < \alpha_{_{V}}, \alpha_{_{l}} < 1$: The cell is at the interface between the liquid and vapor phases.

$$\alpha_{l} + \alpha_{v} = 1 \tag{2}$$

Specifically, the VOF model solves the continuity, momentum, and energy equations as follows: Continuity equation for the VOF model

$$\frac{\partial}{\partial t} (\alpha_l \rho_l) + \nabla \cdot (\alpha_l \rho_l u) = S_{m,l} \tag{3}$$

$$\frac{\partial}{\partial t} (\alpha_{\nu} \rho_{\nu}) + \nabla \cdot (\alpha_{\nu} \rho_{\nu} u) = S_{m,\nu}$$
(4)

here ρ_l is the density of liquid phase and ρ_v is the density of vapor phase. The continuity equations treat velocity u as the mass-averaged velocity. Meanwhile, the rates of mass transfer passing the two-phase interface are represented as $S_{m,l}$ and $S_{m,v}$.

The phase change process can be simulated by assigning source terms to each phase. In the VOF model, only the continuous equation of the secondary phase was solved, while the volume fraction of the primary phase is calculated using Eq. (2). For this study, the vapor phase was considered to be the primary phase, and the liquid phase as the secondary phase. The variables and physical properties

within each cell represent either a single phase or a mixed phase, depending on the volume fraction value. Consequently, only the combined momentum equation and energy equation need to be solved.

Momentum equation for the VOF model

$$\frac{\partial}{\partial t} (\rho u) + \nabla \cdot (\rho u u) = -\nabla p + \nabla \cdot \left[\mu (\nabla u + \nabla u^T) \right] + \rho f_b + F_{CSF}$$
 (5)

here, p is the pressure of mixed phase and f_b represents the centrifugal acceleration. Surface tension plays a crucial role in the movement of bubbles and the wetting characteristics of working fluids. In order to analyze the impact of surface tension on the vapor-liquid interface, the CSF model proposed by Brackbill et al. [27] is implemented as a source term in the momentum equation.

$$\vec{P}_{CSF} = \frac{(\alpha_l \rho_l \kappa_v \nabla \alpha_v + \alpha_v \rho_v \kappa_l \nabla \alpha_l)}{(\rho_l + \rho_v)}$$
(6)

here, κ is the interface curvature.

The rotational centrifugal force is the driving force of the fluid working fluid cycle. It is incorporated into the model as follows

$$f_{bz} = \omega^2 (z + R_0) \tag{7}$$

here, ω is the rotation speed and R_0 is the distance from the condenser end of the RRHP to the axis of rotation.

The energy equation for the VOF model

$$\frac{\partial}{\partial t} (\rho E) + \nabla \cdot [u(\rho E + p)] = \nabla \cdot (k \nabla T) + S_E$$
 (8)

Calculation equation for the physical parameters of mixed phases

$$\rho = \alpha_l \rho_l + (1 - \alpha_l) \rho_v \tag{9}$$

$$\mu = \alpha_l \mu_l + (1 - \alpha_l) \mu_v \tag{10}$$

$$k = \alpha_t k_t + (1 - \alpha_t) k_t \tag{11}$$

$$E = \frac{(\alpha_l \rho_l E_l + \alpha_v \rho_v E_v)}{(\alpha_l \rho_l + \alpha_v \rho_v)}$$
(12)

$$E_{l} = c_{p,l}(T - T_{ref})$$
 (13)

$$E_{v} = c_{p,v} (T - T_{ref}) \tag{14}$$

$$S_E = h_{fg} \cdot S_f \tag{15}$$

Here, E is the mass-averaged internal energy, μ is the mass-averaged dynamic viscosity, and k is the mass-averaged thermal conductivity. $c_{p,l}$ and $c_{p,v}$ represent the specific heat of liquid and vapor.

 S_E is the volumetric mass source term h_{fg} is the latent heat.

2.2 Phase change model

Since the Lee model [28] is more compatible with commercial software as a UDF, it is widely used as the preferred phase change model for heat pipe simulations. The Lee model assumes that mass is transferred at a constant pressure and quasi-thermo-equilibrium state. The phase change process is driven by the deviation between the interface temperature and the saturation temperature. The formula for the volumetric mass source term is as follows:

$$S_{v} = -S_{l} = r_{i,e} \alpha_{l} \rho_{l} \frac{(T - T_{sat})}{T_{sat}} \text{ for evaporation } (T_{sat} < T)$$
 (16)

$$S_{v} = -S_{l} = r_{i,c} \alpha_{v} \rho_{v} \frac{(T - T_{sat})}{T_{sat}} \text{ for condensation } (T_{sat} > T)$$
 (17)

here T is the mixture temperature, $T_{\it sat}$ is the saturation temperature. r_i is the mass transfer intensity factor. While the Lee model aims to minimize the deviation from interface temperature to $T_{\it sat}$, the choice of r_i value shows considerable variability. Previous studies used a broad range of values, ranging from $r_i = 0.1$ to $r_i = 10^7$ [29-35], in order to achieve the highest level of accuracy. The value of r_i is influenced by various factors, including geometry, flow conditions, mesh size and time step. Previous studies have identified potential numerical issues when using the Lee model. If the r_i is too small, it indicates an excessive thermal resistance in the phase change process. A significant deviation between the interfacial temperature and saturation temperature would affect the accuracy of the numerical simulation. To ensure the precision of the simulation model, it was recommended to use a larger value of r_i , which may cause numerical oscillation.

A developed phase change model [36] was utilized to address the numerical oscillation problems when dealing with large $r_{i,c}$ values. Following commissioning, the mass transfer intensity factor in the evaporator section was $r_e = 2$, and $r_c = 2,000,000$ in the condenser section. Additionally, the superheat required for the nucleation process of bubbles was also considered. The expressions for mass transfer rate were given in Eq. (18) – (20). And the energy transfer rate was determined as the product of the mass transfer rate and the latent heat.

If
$$T \ge T_{sat} + \Delta T_i$$

$$S_{v} = -S_{l} = r_{i,e} \alpha_{l} \rho_{l} \frac{(T - T_{sat})}{T_{sat}}$$
 for evaporation (18)

If $T_{sat} < T < T_{sat} + \Delta T_i$

$$S_{v} = -S_{l} = \begin{cases} r_{i,e} \alpha_{v} \rho_{v} \frac{(T - T_{sat})}{T_{sat}}, \alpha_{l} \neq 1, \text{ evaporation} \\ 0, \qquad \alpha_{l} = 1, \text{ neither evaporation nor condensation} \end{cases}$$
(19)

If $T \leq T_{sat}$

$$S_{v} = -S_{l} = r_{i,c} \alpha_{v} \rho_{v} \frac{(T - T_{sat})}{T_{cont}}$$
 for condensation (20)

The location of vapor formation (evaporation), within a liquid or at interfaces, is distinguished via liquid volume fraction α_v . Evaporation takes place in any cell within liquid when it is overheated $(T \geq T_{sat} + \Delta T_i)$, or at the liquid-vapor interfaces $(\alpha_l \neq 1$, the bubble walls and pool surface) once the local temperature rises to the saturation temperature $(T \geq T_{sat})$. And condensation occurs when the temperature decreases below the saturation temperature $(T \leq T_{sat})$, typically at the cooling wall or liquid film surface. The empirical equation for incipient boiling superheat ΔT_i by Hsu [37] was employed.

$$\Delta T_i = \frac{3.06\sigma_{l_v}T_w}{\rho_v h_{fe}\delta} \tag{21}$$

Here, T_w is the wall temperature and δ is the thermal boundary layer thickness.

2.3 Saturation temperature and pressure of the RRHP

The working principle of RRHP is similar to that of a thermosyphon, with one key difference: the driving force of the liquid working fluid reflux, as shown in Figure 2. Therefore, the main distinction between RRHPs and thermosyphons is the saturation temperature and pressure distribution along the heat pipe axis.

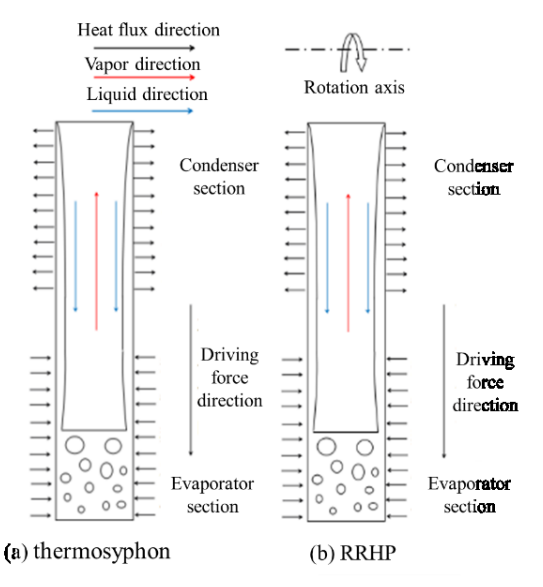


Figure 2. Two-phase closed thermosyphon and RRHP

Assuming that the vapor inside the heat pipe is always in a saturated state, the temperature of the vapor is closely correlated with the pressure. This relationship between temperature and pressure satisfies the Clapeyron equation. The pressure drop of vapor flow inside the heat pipe is as follows:

$$\frac{dp_{v}}{dz} = -\frac{2\tau_{\delta}}{r_{in}} + \rho_{v} f_{b} - \frac{d(r)}{\pi r_{in}^{2} dz}$$
(22)

here, τ_{δ} is the shear force and r_{in} is the inner radius of the RRHP.

The centrifugal driving force of the RRHP is much greater than gravity. Furthermore, both the vapor-liquid phase shear force and vapor pressure drop are independent of the magnitude of the driving force. Therefore, it can be deduced that centrifugal force is the primary factor that causes the axial pressure drop during high-speed rotation. The pressure distribution within the heat pipe can be determined as follows:

$$p_{v} = p_{l,v,pool} - \int_{pool}^{z} \frac{dp_{v}}{dz} dz$$
 (23)

here, $p_{l,v,pool}$ is the pressure at vapor-liquid interface.

In addition, there is a significant pressure difference inside the liquid pool under centrifugal action. As the pressure increases, the required superheat for boiling also increases, and the saturation pressure in the liquid pool area is given by the following equation

$$p_l = p_{v,l,pool} + \int_{r_{pool}}^{r} \rho \omega^2 r dr$$
 (24)

Assuming that all positions along the axial direction of the heat pipe are in a saturated state, the equation for calculating the saturation temperature is as follows

$$T_{sat,r} = f(P_r) \tag{25}$$

3. CFD modelling of the RRHP

3.1 Simulation model of RRHP

A two-dimensional simulation model is developed using geometric parameters derived from turbine disks and compressor disks, along with the standard working temperature range of sodium/potassium heat pipes. Table 1 presents the geometric and working parameters of the heat pipe for numerical simulation. Both the evaporation and condensation sections are 40 mm, with an adiabatic section of 20 mm. Filling ratio is the ratio of the liquid working fluid volume to the evaporation section volume.

Table 1. RRHP parameters

Table 1. NATH parameters.		
Parameters	Materials and values	
Container material	stainless steel	
Working fluid	sodium/potassium	
Length	100 mm	
radius	Inner 6 mm / outer 10 mm	
Centrifugal force	100–10000 g	
Heat flux	120-360 W	
Filling ratio	25%–100 %	

3.2 Initial-Boundary conditions and properties

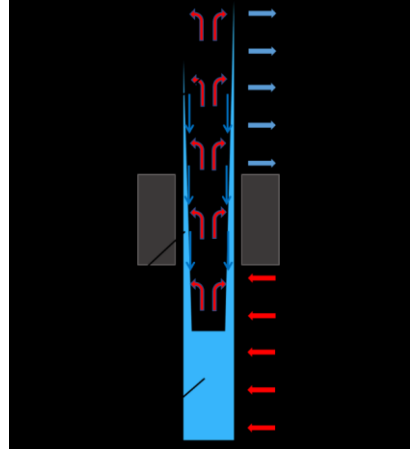


Figure 3. Schematic diagram of the RRHP model

To simulate experimental conditions, the evaporator of the high-temperature RRHP implemented heat flux boundary conditions, while the condenser utilized convection boundary conditions. The convective heat transfer coefficient was obtained from experimental data [18]. The initial filling ratio of the RRHP is set as 50%. For the potassium RRHP, the initial saturation temperature is 873.15 K, while for the sodium RRHP, it is 1073.15 K. Since the main focus of this article is to determine the steady-state working state of the high-temperature RRHP, the initial temperature of the calculation domain was set to the saturation temperature to expedite the solving process. The steady-state working state was determined when the average temperature of different sections no longer changed with time.

Table 2 Physical parameters of liquid sodium and potassium

medium	parameters	formula	Unit
Sodium	ρ	$\rho_{l,Na} = 998.6002 - 2.3192 \times 10^{-1} T + 7.7165 \times 10^{-6} T^2$	kg/m³
	k	$k_{l,Na} = 101.99 - 4.279 \times 10^{-2} T + 9.8809 \times 10^{-7} T^2$	$W/(m \cdot K)$
	C_p	1289.65	$J/(kg \cdot K)$
Potassium	ρ	$\rho_{l,K} = 887.8274 - 2.1199 \times 10^{-1} T + 3.636 \times 10^{-6} T^2$	kg/m³
	k	$k_{l,K} = 78.3222 - 4.865 \times 10^{-2} T + 7.5758 \times 10^{-7} T^2$	$W/(m \cdot K)$
	C_p	757	$J/(kg \cdot K)$

Table 3 Physical parameters of vapor sodium and potassium

medium	parameters	formula	Unit
Sodium	ρ	$\rho_{v,Na} = 8.51351 - 1.806 \times 10^{-2} T + 9.429 \times 10^{-6} T^2$	kg/m³
	k	0.02651	$W/(m \cdot K)$
	c_{p}	904	$J/(kg \cdot K)$
Potassium	ρ	$\rho_{v,K} = 4.30732 - 1.139 \times 10^{-2} T + 7.5167 \times 10^{-6} T^2$	kg/m³
	k	0.0262	$W/(m \cdot K)$
	c_p	5320	$J/(kg \cdot K)$

3.3 Solution strategy and convergence criterion

In this paper, the commercial software ANSYS Fluent 2020R2 was utilized to solve the governing equations. To simulate the vapor-liquid two phase flow heat and mass transfer process, the phase change model compiled by UDF was utilized. The time step size was determined based on the Courant number. In the VOF model, the global maximum Courant number could not exceed 250. For a time-step of 0.001 s, the Courant number of the model would be less than 2. To couple pressure and velocity, the pressure-implicit with the splitting of operators (PISO) scheme was adopted with Skewness-Neighbor corrections of unity. The piecewise linear interface calculation (PLIC) algorithm was used for the volume fraction discretization. Complete details of the solution methods used in this study were provided in Table 4.

Table 4 Solution methods and controls

Discretization method	·
Pressure-	Pressure-implicit with splitting of operators (PISO)
velocity	Skewness correction = 1
coupling	Neighbor correction = 1
Gradient	Least squares cell based
Pressure	Body force weighted
Momentum	First order upwind
Volume fraction	Geo-reconstruct
energy	First order upwind
Transient formulation	First order implicit
Under- relaxation	
factors	
Pressure	0.3
Density	1
Body forces	1
Momentum	0.7
Energy	0.5
Residual	
Continuity	1×10-5
Velocity	1×10-5
Energy	1×10-8

3.4 Mesh Independence Analysis

In this study, the CFD simulation geometry model did not include the length of the connecting section between the stainless-steel tubes. Using ICEM mesh generation software, we constructed the model and divided it into solid wall, solid fin, and fluid domains. Additionally, the RRHP featured boundary layers on the inner wall faces, as illustrated in Figure. 4.

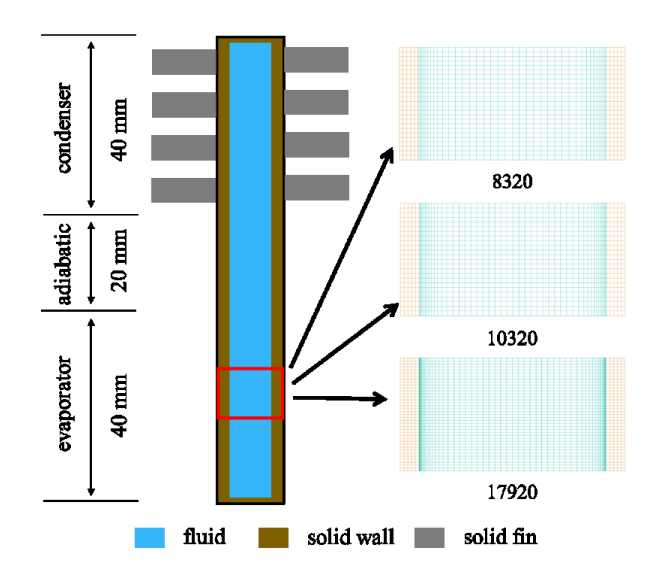


Figure 4. Computational mesh strategies of RRHP

In the grid independence test, four types of grids with different numbers (8320, 10320, 12320, and 17920) were tested, corresponding to the different near-wall grid thicknesses ranging from 0.05 mm to 0.01 mm. The grid independence test was conducted with FR = 50%, a heating flux of 240 W, and sodium as the working fluid. The centrifugal acceleration was set at 1000 g. Table 5 presents the simulation results for the overall temperature difference. It was observed that as the number of grids increased to 12,320, the maximum temperature difference changed by less than 1%. Consequently, a mesh number of 12,320 with a near-wall grid size of 0.02 mm was chosen for the subsequent simulations.

Table 5 mesh independence test for high-temperature RRHP

Mesh number	Thickness of near-wall grid	ΔT_{max} (K)
8320	0.05 mm	58.91
10320	0.03 mm	66.57
12320	0.02 mm	72.09
17920	0.01 mm	72.40

4. Preliminary Results and discussion

This study examined the heat transfer performance and flow state of miniature sodium/potassium RRHPs with different filling ratios under various heating and rotation conditions. The main objective was to simulate the heat and mass transfer process inside the RRHP using the CFD method, and determined the feasibility of combining heat pipes with compressor and turbine disks in aero-engines. Firstly, a series of cases with different centrifugal accelerations were investigated. Then, the influence of filling ratios and heating powers on the RRHP was conducted. Finally, numerical simulation results were used to analyze the effective thermal conductivity of the two types of RRHPs.

4.1 The effect of centrifugal acceleration

In this section, high-temperature RRHPs that used sodium/potassium and had a filling ratio of 50% were simulated under different centrifugal acceleration. The heating power used in the simulations was 240W. The rotational centrifugal acceleration ranging from 100 g to 10000 g were applied to investigate the effect of centrifugal force on miniature sodium/potassium high-temperature RRHPs.

Figure 5 illustrated the temperature distribution of various rotational centrifugal RRHPs. It was clear that there was a slight increase in temperature at the upper part of the evaporator section when the average $f_b = 1000\,\mathrm{g}$. Furthermore, a significant overheating was observed at $f_b = 5000\,\mathrm{g}$, and this

phenomenon became even more pronounced at $f_b = 10000\,\mathrm{g}$. The local overheating in the upper part of the evaporator section was caused by insufficient liquid coverage on the wall surface, leading to dry-out. As the centrifugal acceleration increased, the severity of local overheating gradually escalated. Two main factors contributed to this phenomenon. Firstly, as the centrifugal acceleration increased, the reflux speed of the condensed liquid film accelerated, and the liquid film became thinner. As a result, it became more challenging to form a continuous film. Secondly, the pressure at the bottom of the liquid pool increased, causing the required saturation temperature for boiling to also increase. These changes suppressed the boiling process and reduced the height of the liquid pool. Consequently, the combination of these factors leads to overheating in the upper part of the evaporator section at high centrifugal acceleration.

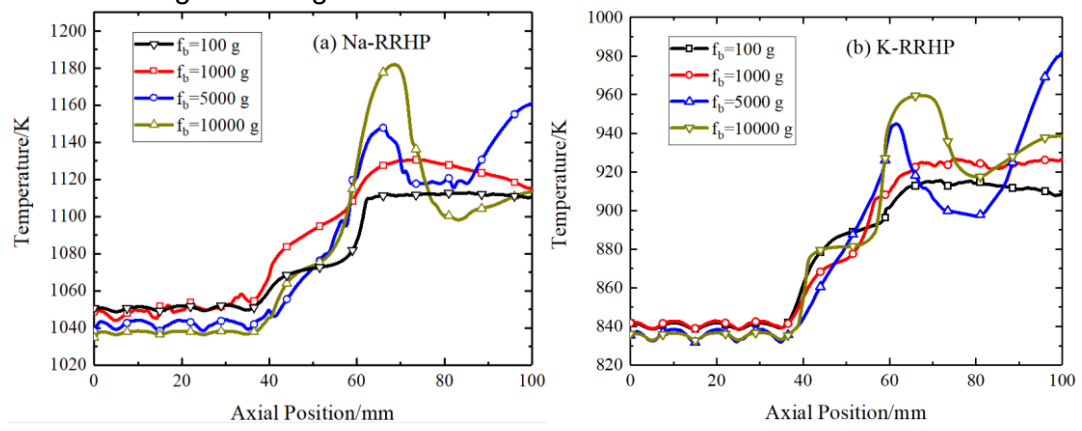


Fig. 5 The temperature distribution with different centrifugal acceleration (a) Na-RRHP and (b) K-RRHP

The Figure 6 visualized the distribution of the vapor-liquid phase in the evaporator section. The red color represented a liquid volume fraction of 1, while the blue color indicated pure vapor. The boiling in the evaporator section of the RRHPs changed significantly with increasing centrifugal acceleration. Additionally, an increase in pressure difference led to a sharp increase in the velocity of the bubbles leaving the liquid surface. The maximum velocity of the vapor in the evaporator section of the heat pipe increased from 1.3 m/s at 100 g to approximately 5 m/s at 10000 g. This change in boiling phenomenon also caused the instability in the vapor velocity at the vapor-liquid surface. The results revealed that a reduction in evaporation bubble formation and the unstable vapor flow at the outlet of the evaporation section may result in the overheating and a large equivalent thermal resistance of the RRHPs at high centrifugal acceleration.

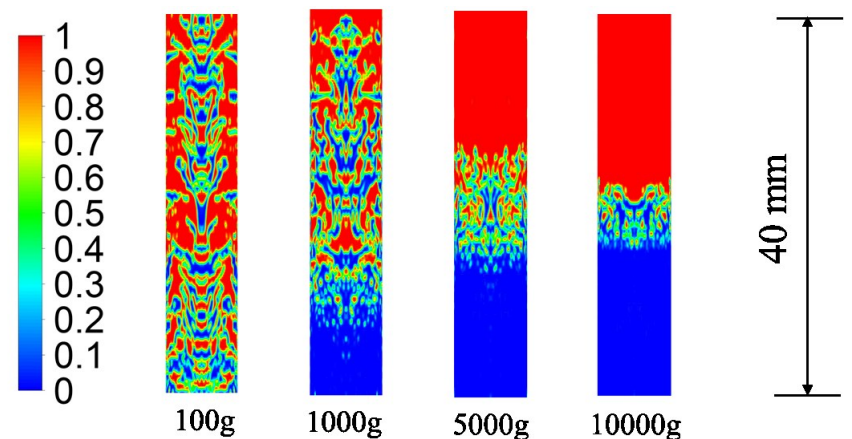


Figure 6. The vapor-liquid distribution of RRHP with different centrifugal acceleration

The thermal resistance comparison of two different types of high-temperature RRHPs under different rotational centrifugal accelerations was illustrated in Figure 7. As the centrifugal acceleration increased, the overall thermal resistance of the heat pipe also increased. Specifically, when the

rotational centrifugal acceleration increased from 100 g to 10000 g, the thermal resistance increases by approximately 32%. This increase could be attributed to two factors. On the one hand, this was a decrease of temperature within the condenser section, and on the other hand, a temperature jump phenomenon occurred in the upper part of the evaporator section, resulting in a larger temperature difference between the evaporator and condenser sections. However, it was important to note that a higher rotational centrifugal force would not cause the RRHPs failure.

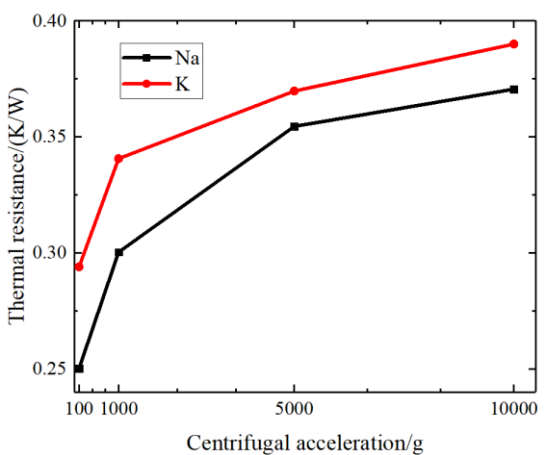


Figure 7. The thermal resistance of Na-RRHP and K-RRHP with different centrifugal acceleration

4.2 The effect of filling ratios

To address the issue of local overheating at high speeds, the filling ratios were study in this section. Simulations were performed using sodium high-temperature RRHPs with filling ratios of 25%, 50%, 75%, and 100% were simulated. The simulations were conducted under identical initial and boundary conditions, with $f_b = 5000 \, \mathrm{g}$ and a heating power of 240W.

As shown in Figure 8, a significant overheating was observed in most areas of the evaporator section when the filling ratio was 25%. This overheating greatly compromised the heat transfer performance of the RRHP. Even at a 50% filling ratio, there was still noticeable overheating in the upper part of the evaporator section. Additionally, the highest temperature recorded at the bottom of the liquid pool. Increasing the filling ratio to 75% and 100%, the overheating phenomenon no longer occurred. However, as the filling ratio increased, the pressure at the bottom of the liquid pool continued to rise, resulting in gradual suppression of pool boiling. The highest temperature in the RRHP remained at the bottom of the liquid pool. Furthermore, increasing the filling ratio did not significantly impact in the temperature of the condenser section. This indicated that changes in filling ratios would not impact the operation of the condenser section.

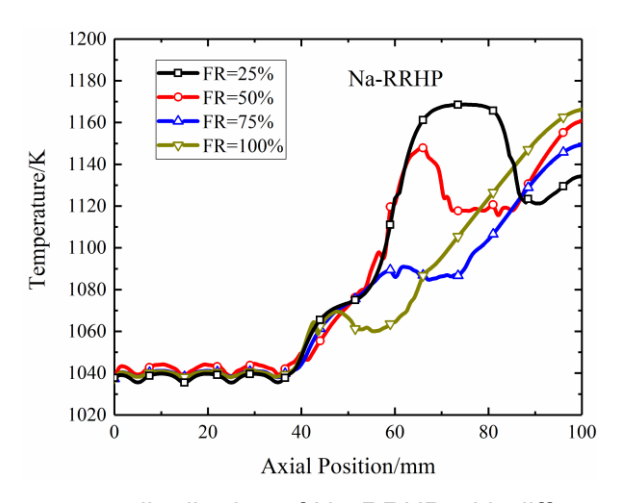


Figure 8 The temperature distribution of Na-RRHP with different filling ratios

The comparison of the total thermal resistance of high-temperature RRHPs at different filling ratios was shown in Figure 9. As the filling ratio increased, the total thermal resistance initially decreased and then increased. When the filling ratio increased from 25% to 75%, the thermal resistance increased by approximately 35%. This was because the reflux of the liquid film inside the heat pipe was affected by the height of the liquid pool. When the RRHP filling ratio was 100%, its equivalent thermal resistance would increase from 0.2942 K/W to 0.34216 K/W. This change in equivalent thermal resistance was caused by local overheating at low filling ratios and excessive saturation pressure at high filling ratios. These findings highlight the importance of selecting an appropriate filling ratio to enhance the overall heat transfer efficiency of the RRHP under the current operating conditions.

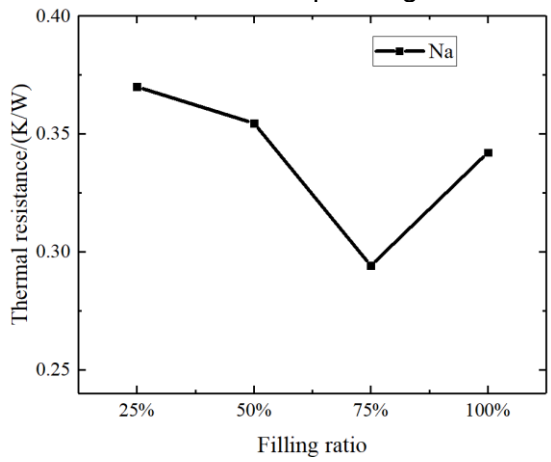


Figure 9. The thermal resistance of Na-RRHP with different filling ratios

4.3 The effect of heating power

In this section, simulations were conducted to explore the impact of different thermal load conditions on high-temperature RRHPs with various heating powers. The centrifugal acceleration was set at $f_b = 1000\,\mathrm{g}$, and the filling ratio was 50%. The evaporator section was exposed to heating powers of 120 W, 240 W, and 360 W, while the boundary conditions of the condenser section were adjusted accordingly.

As shown in Figure 10, the temperature of the evaporator section gradually increased and the evaporation velocity rate accelerated as the heating power increased. The temperature difference between the wall and the vapor core also increased, leading to an acceleration in the condensation velocity rate. Moreover, the overall phase change rate of the RRHP increased with the increase in heating power, resulting in a faster working fluid circulation and enhanced heat transfer. However, at low heating power (Q=120 W), the RRHP did not reach its ideal working state. This was characterized by the significant temperature difference within the evaporation section, indicating the absence of nucleate boiling in the liquid pool.

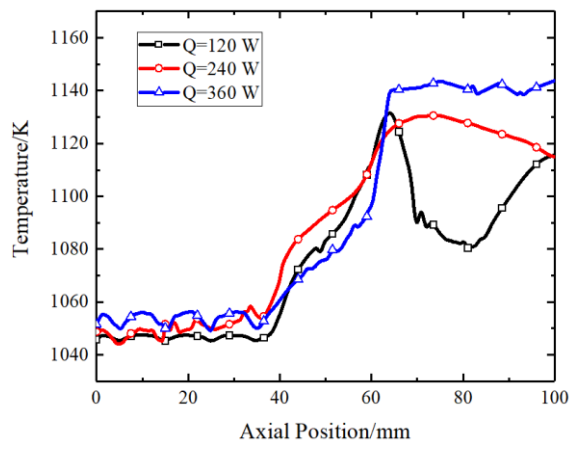


Figure 10 The temperature distribution of Na-RRHP with different heating powers

As shown in Figure 11, the total thermal resistance of the RRHP exhibited a downward trend as the heating power increased. When the heating power increased from Q=120 W to Q=360 W, the thermal resistance decreased by approximately 45%. Furthermore, the difference in thermal resistance between Q=240 W and Q=360 W was less than 15%, indicating that the RRHP achieved optimal working conditions. The minimum equivalent thermal resistance of the heat pipe could reach 0.2410 K/W. As the heating power increased, the working state of the heat pipe became more stable, resulting in a stabilization of the thermal resistance. Overall, by increasing the heating power within the heat transfer limit, the phase change and working fluid circulation rate inside the RRHP improved, leading to a decrease in the total thermal resistance and an enhancement in working efficiency. These findings suggest that the RRHP was highly suitable for high heating power environments and held promising potential for application in aero-engines.

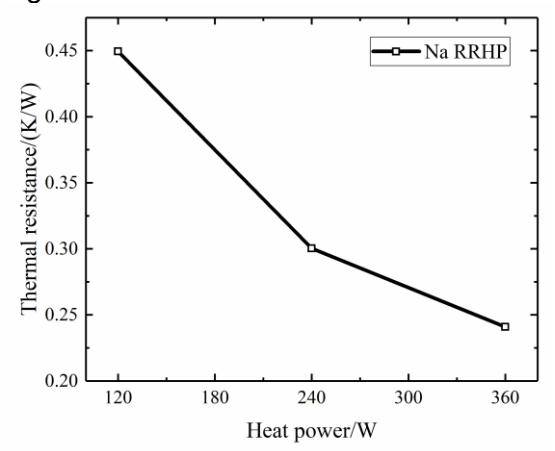


Figure 11. The thermal resistance of Na-RRHP with different heating powers

4.4 Heat transfer analysis of the RRHPs

In order to assess the thermal performance of the RRHPs filled with working fluid, the heat transfer capability was modeled as a solid cylinder of equal size. The effective thermal conductivity $k_{\rm eff}$ of this solid cylinder was determined using the following correlation:

$$k_{\text{eff}} = \frac{4L}{d_0^2} \left[\frac{\ln(d_0/d_i)}{2(L_e/L)} + \frac{k_W}{h_e d_0(L_e/L)} + \frac{k_W}{h_c d_0(L_c/L)} + \frac{\ln(d_0/d_i)}{2(L_c/L)} \right] k_W$$
 (26)

here, L, L_e , L_c are the lengths of RRHP, evaporator and condenser respectively. d_0 and d_i are the outer diameter and inner diameter respectively. and k_W is the thermal conductivity of the wall. h_e and h_c represent the heat transfer coefficients of the evaporator and the condenser with the following forms, respectively:

$$h_e = \frac{Q}{\pi d_0 L_e (T_e - T_{sat})}$$
 (27)

$$h_c = \frac{Q}{\pi d_0 L_c (T_{sat} - T_c)} \tag{28}$$

here T_e and T_c are the average wall temperatures of the evaporator and the condenser, respectively, and Q represents the power input.

The Figure 12 showed the effective thermal conductivity of the RRHP at various centrifugal accelerations. It was evident that the largest effective thermal conductivity occurred at lower centrifugal accelerations. As the speed increased, it gradually stabilized. As shown in Figure 12 (a), the effective thermal conductivity of Na-RRHP and K-RRHP at $f_b = 10000 \, \mathrm{g}$ were 2606 W/m·K and 2252 W/m·K, respectively. Since the RRHPs were embedded in the turbine disk or compressor disk, the disk itself served as the heat pipe shell. Therefore, further calculations of the equivalent thermal conductivity without a shell were also conducted. As shown in Figure 12 (b), the effective thermal conductivity of

Na-RRHP and K-RRHP were 9176 W/m·K and 8966 W/m·K, respectively. This study revealed that the effective thermal conductivity of the RRHPs was more than 20 times higher than that of copper and approximately 500 times higher than that of stainless steel.

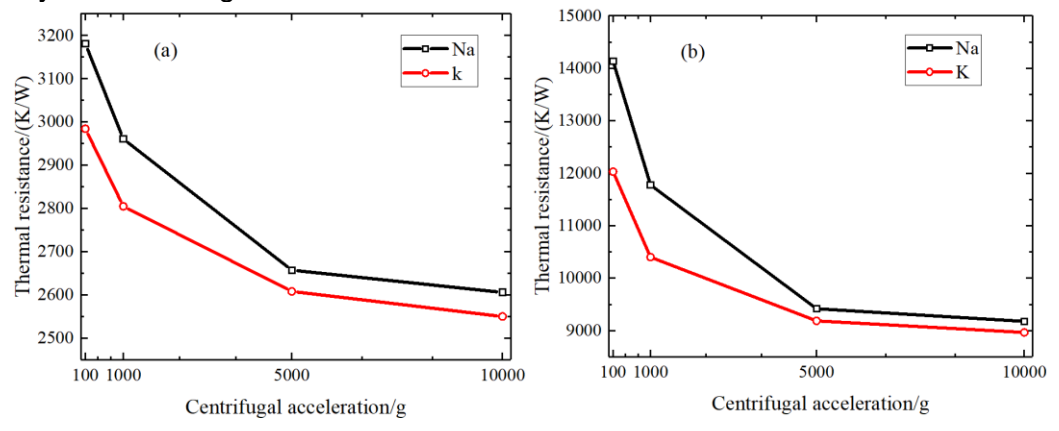


Figure 12. The effective thermal conductivity of RRHP with different centrifugal acceleration (a) including RRHP shell (b) excluding RRHP shell

5. Preliminary Conclusions

In this study, the flow state of working fluid and the heat transfer mechanism in miniature high temperature RRHPs were investigated. The results indicated that the CFD model was effective in accurately predicting the two-phase flow and heat transfer characteristics. The heat transfer performance of miniature Sodium/Potassium RRHP under different centrifugal accelerations, heating powers, and filling ratios was conducted. The preliminary research conclusions were as follows:

- 1) The thermal resistance of the RRHPs increased with the rotating speed, but the overall increase in thermal resistance did not exceed 35%. Under lower centrifugal acceleration conditions, the temperature distribution of the heat pipe tended to remain steady. As the centrifugal acceleration increased, the RRHPs experienced local overheating. However, even under high centrifugal force, the heat pipes were still able to maintain excellent heat transfer performance.
- 2) When the liquid filling ratios of the RRHPs were lower (25% and 50%), areas without condensate cooling were observed on the upper part of the evaporator section, leading to a localized overheating. This study found that the RRHP performed optimally with a liquid filling ratio of 75% at $f_b = 5000 \, \mathrm{g}$.
- 3) For the same RRHP, the overall thermal resistance decreased as the heating flux increased. This is because the centrifugal driving force of the RRHPs is significantly higher than gravity, indicating that RRHPs are less affected by the flooding limit. The optimal equivalent thermal conductivity under $f_b = 1000 \, \mathrm{g}$ working condition was 0.24096 K/W at heating power of 360 W.
- 4) Both the equivalent thermal resistance and effective thermal conductivity were investigated for the RRHP with a filling ratio of 50%, and a heating power of 240 W at $f_b = 10000\,\mathrm{g}$. The thermal resistance values were found to be 0.37059 K/W and 0.38924 K/W for Na-RRHP and K-RRHP, respectively. As for the effective thermal conductivity, it was determined to be 2606 W/m·K and 2252 W/m·K for Na-RRHP and K-RRHP including the RRHP shell. Excluding the RRHP shell, the effective thermal conductivity values were 9176 W/m·K for Na-RRHP and 8966 W/m·K for K-RRHP.

This research indicated that arranging embedded heat pipes could lead to a reasonable redistribution of disk energy, reducing the thermal stress, and lowering the maximum temperature. This achievement would contribute to improving both engine performance and safety. However, it was important to note that the heat transfer performance may deteriorate significantly due to the saturation pressure difference along the axis. Therefore, when designing the heat pipe structure, efforts should be made to increase the area of the evaporator section while reducing its length. It was crucial to avoid local overheating, as it could occur with an unreasonable design of the embedded heat pipes. This was particularly important when applying high-temperature heat pipes in aero-engine turbine disks or compressor disks.

Copyright Statement

The authors confirm that they, and/or their company or organization, hold copyright on all of the original material included in this paper. The authors also confirm that they have obtained permission, from the copyright holder of any third party material included in this paper, to publish it as part of their paper. The authors confirm that they give permission, or have obtained permission from the copyright holder of this paper, for the publication and distribution of this paper as part of the ICAS proceedings or as individual off-prints from the proceedings.

References

- [1] Zhou Z Y, Li H W, Wang H C, et al. Rotating Film Cooling Performance of the Hole Near the Leading Edge on the Suction Side of the Turbine Blade. *ASME 2018 International Mechanical Engineering Congress and Exposition*, Pittsburgh, Pennsylvania, USA, 86929, 2018.
- [2] CFR 14 Part 33 Airworthiness standards Aircraft Engines, Federal Aviation Administration Department of Transportation, pp 33.1-33.201
- [3] Cao Y Z. Aeroengine heat transfer. Beihang University Press, 2005.
- [4] Fu D, Ding S, Tao Z, et al. Correlation analysis of rotating disk stress level and temperature distribution[J]. *Journal of Aerospace Power*, Vol. 23, No. 4, pp 623-628, 2008.
- [5] Owen J M, Powell J. Buoyancy-Induced Flow in a Heated Rotating Cavity. *Journal of Engineering for Gas Turbines and Power*, Vol. 128, pp 128-134, 2006.
- [6] Farzaneh-Gord M, Wilson M, Owen J M. Numerical and Theoretical Study of Flow and Heat Transfer in a Pre-Swirl Rotor-Stator System. *Proceedings of Turbo Expo 2005: Power for Land, Sea and Air*. Nevada, USA: ASME, 2005: GT2005-68135.
- [7] Farzaneh-Gord M. Heat Transfer over Rotor Surface in a Pre-Swirl Rotating-Disc System. *International Journal of Dynamics of Fluids*, Vol. 3, No 1, pp 81-94, 2007.
- [8] Ni M, Zhu H R, Qiu Y, et al. Overview of the cooling technology of aero-engine turbine blade. *Gas Turbine Technology*, Vol. 18, No 4, pp 25-33,2005
- [9] Bunker R S. Gas turbine heat transfer: ten remaining hot gas path challenges. *Journal of Turbomachinery*, Vol. 129, No. 2, pp 193-201,2007
- [10]Cao Y, Ling J. Performance Simulations of a Gas Turbine Disk-Blade Assembly Employing Miniature Radially Rotating Heat Pipes. *Journal of Heat Transfer*, Vol. 134, No 5, pp 051016, 2012.
- [11]Ding S., Luo B. Control of Stress in Aeroengine Turbine Disk Using Radially Rotating Heat Pipe, *Journal of Thermophysics and Heat Transfer*, Vol 28, No 3, pp 428-439, 2014.
- [12]Ling J, Cao Y. Experimental Investigations of a Radially Rotating Miniature High–Temperature Heat Pipes, *ASME J. Heat Transfer*, Vol. 121, No 1, pp 113-119, 2001.
- [13]Cao Y, Ling J, Rivir R, et al. A Numerical Analysis of Gas Turbine Disks Incorporating Rotating Heat Pipes. *ASME-PUBLICATIONS-HTD*, Vol. 366, pp 61-68, 2000.
- [14]Eisenmann S, Schmidt T, Gümmer V, et al. Fatigue Analysis of a Cylindrical Turbine Disk with Integrated Heat Pipes, 52nd AIAA/SAE/ASEE Joint Propulsion Conference. American, 2016
- [15]Taamneh Y. Thermal analysis of gas turbine disk integrated with rotating heat pipes. Case Studies in *Thermal Engineering*, Vol. 10, pp 335-342, 2017.
- [16] Tian Z X, Wang C L, Guo K L. A review of liquid metal high temperature heat pipes: Theoretical model, design, and application. *International Journal of Heat and Mass Transfer*, Vol 214, pp 124434, 2023.
- [17]Reay D A, Kew P. Heat pipes. 5th ed . Oxford, UK: Butterworth-Heinemann, 2006.
- [18]Ling J, Chang W S, Cao Y. Analyses of Radially Rotating High-Temperature Heat Pipes for Turbomachinery Applications. *Journal of Engineering for Gas Turbines and Power*, Vol. 121, No 2, pp 306-312, 1999.
- [19]Chen J , Fu Y , He Q ,et al. Environmentally friendly machining with a revolving heat pipe grinding wheel. *Applied Thermal Engineering*, Vol 107, pp:719-727, 2016.
- [20]Qian N, Jiang F, Marengo M, et al. Thermal performance of a radial-rotating oscillating heat pipe and its application in grinding processes with enhanced heat transfer. *Applied Thermal Engineering*, Vol 233, pp 121213,2023.
- [21]Luo F Q, Ma C, Liu J L, et al. Effect of gas—liquid phase change of axial rotating heat pipe on fluid-thermal-solid behaviors of high-speed spindle. *Applied Thermal Engineering*, Vol 232, pp 121117, 2023.

- [22]Sun H, Pellegrini M, Wang C, et al. CFD simulation based on film model of high temperature potassium heat pipe at different positions: Horizontal, vertical, and 45° inclined. *Progress in nuclear energy*, 2022.
- [23]Sun H , Tang S , Wang C, et al. Numerical simulation of a small high-temperature heat pipe cooled reactor with CFD methodology. *Nuclear Engineering and Design*, Vol. 370, pp 110907,2020.
- [24] Dutra C, Merzari E, Ahn T, et al. High fidelity modeling and experiments to inform safety analysis codes for heat pipe microreactors. *Nuclear Technology*, Vol. 209, pp 1592-1616, 2023.
- [25]Zhang Z, Chai X, Wang C, et al. Numerical investigation on startup characteristics of high temperature heat pipe for nuclear reactor. *Nuclear Engineering and Design*, Vol. 378, No 1, pp 111180, 2021
- [26]Hirt C W, Nichols B D. Volume of Fluid (VOF) Method for The Dynamics of Free Boundaries[J]. Journal of Computational Physics, Vol. 39, No. 1, pp 201-225, 1987.
- [27]Brackbill J U, Kothe D B. Zemach C. A Continuum Method for Modeling Surface Tension[J]. Journal of Computational Physics, Vol. 100, pp 335-354, 1992.
- [28]Lee W H. Pressure iteration scheme for two-phase flow modeling. *Multiphase Transport: Fundam-Entals, Reactor Safety, Applications*, pp 407-432, 1980.
- [29]Min W D, Zhong W, et al. Investigation of the condensation mass transfer time relaxation parameter for numerical simulation of the thermosyphon. *International Journal of Heat and Mass Transfer*, Vol. 201, pp 123599, 2023.
- [30]Wang X, Zhu Y, Wang Y. Development of pressure-based phase change model for CFD modelling of heat pipes. *International Journal of Heat and Mass Transfer*, Vol. 145, pp 118763, 2019.
- [31] Fang C, David M, Rogacs A, et al., Volume of fluid simulation of boiling two-phase flow in a vapor-venting microchannel, *Frontiers in Heat and Mass Transfer*, Vol. 1, No. 1, pp 013002, 2010.
- [32]Riva E D, Col D D. Effect of gravity during condensation of r134a in a circular mini-channel. *Microgravity Science and Technology*, Vol. 23, No. 1 Supplement, pp 87-97, 2011.
- [33]You Y W, Wang G, Guo C M, et al. Study on mass transfer time relaxation parameter of indirect evaporative cooler considering primary air condensation, *Applied Thermal Engineering*, Vol. 181, pp 115958, 2020.
- [34]Lei Y, Mudawar I, Chen Z. Computational and experimental investigation of condensation flow patterns and heat transfer in parallel rectangular micro-channels. *International Journal of Heat and Mass Transfer*, Vol. 149, No. 4, pp 119158, 2020.
- [35]Li G, Zhang Y C, Zhang G H, et al. Transient experimental and numerical study of thermosyphon under different heating fluxes and filling ratios, *Applied Thermal Engineering*, Vol. 243, pp 122514, 2024.
- [36]Zhang Y C, Li G, Zhang G H, et al. Development and modified implementation of Lee model for condensation simulation, *Applied Thermal Engineering*, Vol. 231, pp 180872, 2023.
- [37] Hsu Y Y. On the size range of active nucleation cavities on a heating surface, *Journal of Heat Transfer*, Vol. 84, pp 207, 1962.